High-Resolution Real-Time Imaging Processing for Spaceborne Spotlight SAR With Curved Orbit via Subaperture Coherent Superposition in Image Domain

Yanbin Liu, *Student Member, IEEE*, Guang-Cai Sun, *Senior Member, IEEE*, Liang Guo, Mengdao Xing, *Fellow, IEEE*, Hanwen Yu, *Senior Member, IEEE*, Ruimin Fang, and Shiyu Wang

***Abstract*—With the increasing of application requirements, the high-resolution real-time imaging processing of the spaceborne spotlight synthetic aperture radar (SAR) has been developed. Since the traditional real-time imaging algorithms have the problems that the range model has errors and the two-dimensional (2-D) space-variance of the equivalent velocity caused by the curved orbit cannot be effectively eliminated. Thus, this article proposes a high-resolution real-time imaging algorithm for spaceborne spotlight SAR with curved orbit via subaperture coherent superposition in image domain. In this article, the echo data are first divided into subapertures to avoid the azimuth spectrum aliasing. After that, the 2-D space-variance of the equivalent velocity caused by the curved orbit can be eliminated by the method of azimuth time scale transformation, higher order phase compensation, and introducing phase transition function. Then, the dechirp function is applied for the subaperture signals to obtain the partial-resolution subaperture images. Finally, these partial-resolution subaperture images are coherently superposed in the image domain to obtain the final full-resolution image of the whole echo data. Moreover, the proposed algorithm improves the real-time performance by adopting the idea that the subaperture data recording and subaperture real-time imaging processing are synchronized, which greatly accelerates the acquisition of the final full-resolution imaging result. At the end of this article, the simulations and the real-time performance analysis are performed to validate the proposed algorithm.**

***Index Terms*—Curved orbit, high-resolution real-time imaging, spaceborne synthetic aperture radar (SAR), spotlight mode, subaperture coherent superposition.**

Manuscript received October 23, 2021; revised January 14, 2022; accepted February 4, 2022. Date of publication February 10, 2022; date of current version March 2, 2022. This work was supported in part by the National Key R&D Program of China (the foundation strengthening project) under Grant 2018YFA0701903, in part by the State Key Program of National Natural Science of China under Grant 61931025, in part by the National Science Fund for Distinguished Young Scholars under Grant 61825105, and in part by the Key Scientific and Technological Innovation Team Foundation of Shannxi under Grant 2019TD-002. *(Corresponding author: Guang-Cai Sun.)*

Yanbin Liu, Liang Guo, and Shiyu Wang are with the School of Physics and Optoelectronic Engineering, Xidian University, Xi'an 710071, China (e-mail: ybliu_rsp@163.com; lguo@mail.xidian.edu.cn; yshi@mail.xidian.edu.cn).

Guang-Cai Sun and Ruimin Fang are with the National Laboratory of Radar Signal Processing, Xidian University, Xi'an 710071, China (e-mail: rsandsgc@126.com; fangruimin9802@163.com).

Mengdao Xing is with the National Laboratory of Radar Signal Processing, Xidian University, Xi'an 710071, China, and also with the Academy of Advanced Interdisciplinary Research, Xidian University, Xi'an 710071, China (e-mail: xmd@xidian.edu.cn).

Hanwen Yu is with the School of Resources and Environment, University of Electronic Science and Technology of China, Chengdu 611731, China (e-mail: yuhanwenxd@gmail.com).

Digital Object Identifier 10.1109/JSTARS.2022.3150025

I. Introduction

As AN active microwave imaging system, spaceborne synthetic aperture radar (SAR) is able to perform the two-dimensional (2-D) imaging in all-weather and all-day conditions [1]–[7]. With its superior global observation capability, spaceborne SAR has been widely used in some applications such as topographic mapping, resource detection, disaster monitoring, and target recognition [8]–[12]. With the increasing of application requirements, the spaceborne SAR technology is developing quickly. To quickly and efficiently complete some urgent observation tasks, the spaceborne SAR is required to carry out the high-resolution and real-time observation for specific areas, so the high-resolution real-time imaging processing for the spotlight imaging mode is developed in the spaceborne SAR technology [13]–[16]. However, in the case of high-resolution real-time imaging of the spaceborne spotlight SAR, the long synthetic aperture time makes the trajectory of the spaceborne SAR more complicated and the data volume of the echo signal increase sharply [17], [18], which bring great challenges to the high-resolution real-time imaging. As we know large data take a long time to transmit, so it is not appropriate to directly transmit the echo data in the high-resolution real-time spaceborne SAR imaging. In contrast, a more effective method is to first process the echo data by using the high-resolution real-time imaging algorithms, then store the imaging result as an image with a size of several *m* bytes, finally transmit the image to the ground, which will save a lot of time than the direct transmission of the echo data. The core of high-resolution real-time imaging processing for the spaceborne spotlight SAR is to generate the high-quality imaging results as quickly as possible after the echo data recording is completed [19]–[22]. Under the condition that the existing hardware configurations are already advanced, it may take more research and development costs to accelerate the generation of the high-quality imaging results by seeking improvements and updates on the hardware. Therefore, it is a good choice to seek breakthroughs in the high-resolution

real-time imaging algorithms to generate high-quality imaging results as quickly as possible.

There are three main problems that can be solved in the high-resolution real-time imaging algorithms for the spaceborne spotlight SAR with curved orbit. The first problem is the azimuth spectrum aliasing caused by the condition that the azimuth signal bandwidth is greater than the pulse repeating frequency (PRF) in the spaceborne spotlight SAR. The second problem is the space-variance of the equivalent velocity caused by the curved orbit. In the high-resolution spaceborne SAR imaging, the real orbit of the spaceborne SAR is curved due to the long synthetic aperture time. The curved orbit and the curved surface of the earth make the velocity in the spaceborne SAR imaging and is no longer the real physical velocity, but the selected virtual velocity, also known as the equivalent velocity [1]. And the 2-D space-variance of the equivalent velocity caused by the curved orbit cannot be ignored, making the traditional range model based on the straight orbit no longer accurate. The third problem is how to improve the real-time performance of the imaging processing and shorten the waiting time of obtaining the final imaging results after the echo data recording is completed. For the first problem that the azimuth spectrum aliasing occurs in the spaceborne spotlight SAR, many traditional imaging algorithms such as the polar format algorithm (PFA) [23], the wide-field PFA, the differential Doppler algorithm, the stolt PFA (SPA) [24], [25], the two-step processing approach [26], the focusing algorithm based on the fractional Fourier transform [27], and the frequency scaling algorithm with subaperture division [28] have been proposed to effectively deal with it. However, above imaging algorithms are based on the traditional hyperbolic range model (HRM) without considering the curved orbit, thus they are not valid in the high-resolution real-time imaging processing for the spaceborne spotlight SAR.

For the second problem that the space-variance of the equivalent velocity is caused by the curved orbit in the high-resolution spaceborne SAR imaging, some new range models and imaging algorithms are proposed. A subaperture imaging algorithm considering the azimuth space-variance of the equivalent velocity is proposed in [29] for the ultrahigh-resolution spaceborne sliding spotlight SAR. However, there needs a complex azimuth position regulation in the subaperture recombination because each subaperture has different model parameters. In addition, some imaging algorithms based on the motion compensation are proposed in [30], [31] to compensate the real curved orbit into an approximate straight orbit. However, the accuracy of the compensation is affected by the azimuth scene size [32]. Furthermore, a high-order imaging algorithm based on the modified equivalent squint range model (MESRM) is proposed in [33]. However, the MESRM does not consider the azimuth space-variance of the equivalent velocity caused by the curved orbit. Another new range model called the sixth-order Doppler parameter range model is proposed in [34], and the back-projection algorithm (BPA) is chosen for imaging processing. However, the BPA is not suitable for real-time imaging processing due to its long processing time and large computation. Moreover, the equivalent acceleration range model (EARM) considering the curved orbit is proposed in [32]. However, the stolt interpolation in [32] requires a lot of processing time.

As for the third problem about improving the real-time performance of the imaging processing, some real-time imaging algorithms are proposed. The real-time imaging algorithm in [21], [22], [35] are proposed for the spaceborne stripmap SAR without considering the azimuth spectrum aliasing and the curved orbit, and thus they are not able to use in the high-resolution real-time imaging processing for the spaceborne spotlight SAR. In addition, a real-time processing method based on variable PRF is proposed in [16]. However, that method is not suitable for directly processing the spaceborne spotlight SAR data and does not consider the range space-variance of the equivalent velocity. Moreover, a real-time imaging method based on the modified range migration algorithm (RMA) is proposed in [15] for spaceborne spotlight SAR. However, the stolt interpolation takes a lot of time. And the range model in it has the errors because of not considering the curved orbit, thus resulting in a poor focus in the imaging result of the high-resolution spaceborne spotlight SAR.

To solve above three main problems, this article proposes a high-resolution real-time imaging algorithm for spaceborne spotlight SAR with curved orbit via subaperture coherent superposition in image domain. In the proposed algorithm, the echo data are first divided into subapertures, and the azimuth spectrum aliasing is avoided because the azimuth signal bandwidth of each subaperture data is much smaller than the PRF. Then, according to the new subaperture range model considering the curved orbit, the azimuth space-variance of the equivalent velocity can be eliminated by the method of azimuth time scale transformation and higher order phase compensation. After using chirp scaling algorithm (CSA) to complete the range processing, the phase transition function is introduced to convert the hyperbolic azimuth phase to the quadratic phase and eliminate the range space-variance of the equivalent velocity. And then, the dechirp function is used for the subaperture signals to obtain the partial-resolution subaperture images. Finally, these partial-resolution subaperture images are coherently superposed in the image domain to obtain the full-resolution image of the whole echo data.

Compared with the full-aperture algorithms, the subaperture algorithms is more suitable for parallel real-time processing. Traditional subaperture algorithms mostly perform subaperture recombination in the signal domain before focusing processing [28]–[30], [32], [36], while the proposed algorithm performs the subaperture coherent superposition in the image domain after the subaperture focusing. The difference between the traditional subaperture algorithms and the proposed algorithm is shown in Fig. 1. Traditional subaperture algorithms usually need a long azimuth Fourier transform (FT) operation and phase compensation to complete the complex focusing processing of a long signal after subaperture recombination, and then obtain the final imaging result. While the proposed algorithm uses the simple addition operation in the image domain to complete the subaperture coherent superposition, thereby obtaining the final full-resolution image. That is to say, compared with the

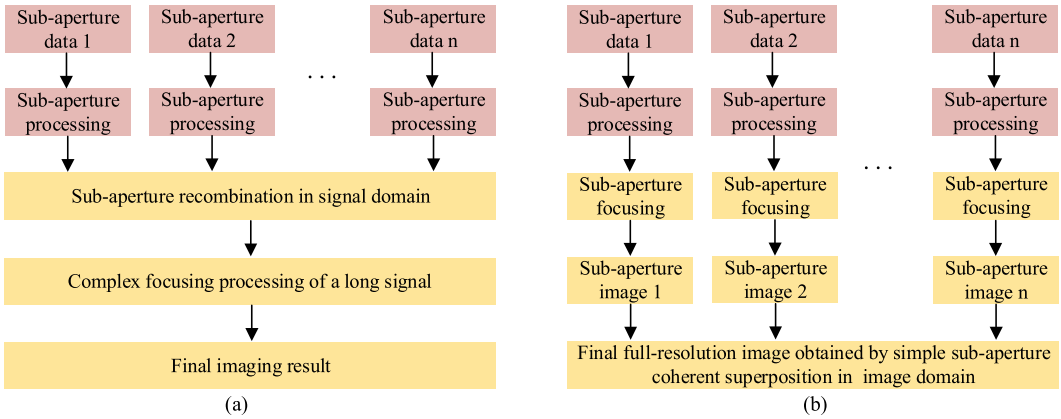

Fig. 1. Difference between the traditional subaperture algorithms and the proposed algorithm. (a) Traditional subaperture algorithms. (b) Proposed algorithm.

traditional subaperture algorithms, the proposed algorithm splits the complex focusing processing of a long signal into the simple coherent superposition of several subaperture images, which means that the long azimuth FT operation is replaced by the addition operation, and the computational burden of the addition operation is less than that of long FT operation.

The proposed algorithm focuses on how to quickly obtain spaceborne SAR high-resolution imaging results. The proposed algorithm combines the slant range model of curved orbit with the new method of subaperture coherent superposition in image domain that is different with the traditional subaperture algorithms, so that the subaperture data recording and subaperture real-time imaging processing are performed simultaneously in the high-resolution spaceborne SAR imaging. In other words, the real-time imaging processing of the first subaperture data is completed within the recording time of the second subaperture data. By analogy, the real-time imaging processing of the penultimate subaperture data is completed within the recording time of the last subaperture data. Thus, when all the data have been recorded, only the last subaperture data remains to be processed, and the final full-resolution image can be obtained as long as waiting for the imaging processing time of the last subaperture data. The purpose of the real-time imaging processing is to obtain the final high-quality imaging result as quickly as possible. After all the data have been recorded, the proposed algorithm can shorten the waiting time of obtaining the final full-resolution imaging result to the imaging processing time of the last subaperture data, which greatly accelerates the acquisition of the final full-resolution imaging result and effectively realizes the high-resolution real-time imaging processing. Compared with the traditional algorithms, the proposed algorithm in this article can realize the high-resolution spaceborne SAR imaging and on-board real-time imaging simultaneously.

The rest of this article is organized as follows. Section II establishes the new subaperture signal model considering the curved orbit. The algorithm flow chart and the formulas derivation are presented in detail in Section III. Section IV presents the simulation results and analyze the real-time performance of the proposed algorithm by using the TMS320C6678 digital signal processor (DSP). Finally, Section V concludes this article.

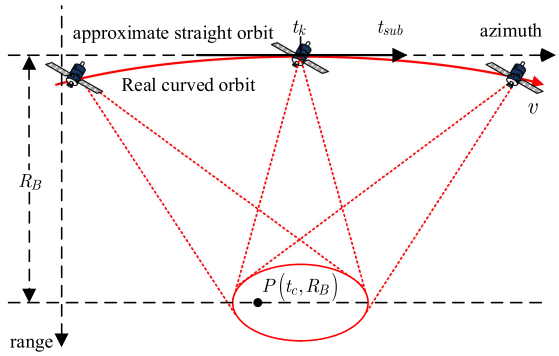

Fig. 2. Geometry of subaperture data recording in spaceborne spotlight SAR.

II. Subaperture Signal Model

The new range model called EARM proposed in [32] considers the curved orbit. On this basis, the subaperture signal model is derived in this part. The geometry of the subaperture data recording in spaceborne spotlight SAR is depicted in Fig. 2. t_k is the central moment of the kth subaperture data, $t_{\rm sub}$ is the azimuth time of the subaperture data, and v is the equivalent velocity of the spaceborne SAR. In the low-resolution spaceborne SAR imaging, the trajectory of the spaceborne SAR could be approximated as a straight orbit shown in the Fig. 2. And thus according to the HRM, the sensor-target distance of an arbitrary point target $P(t_c, R_B)$ can be expressed as

$$R_{\rm hrm}\left(t_{\rm sub}\right) = \sqrt{{R_B}^2 + \left(v\left(t_k + t_{\rm sub} - t_c\right)\right)^2}. \tag{1}$$

However, the actual orbit of the spaceborne SAR is curved as the synthetic aperture time becomes longer in the high-resolution spaceborne SAR imaging, making (1) based on the straight orbit no longer accurate. Curved orbit will make the equivalent velocity change along the azimuth direction, that is, azimuth space-variance of the equivalent velocity. To describe the azimuth space-variance of the equivalent velocity, the equivalent acceleration is introduced in [32] and the spaceborne SAR is regarded as moving with a constant acceleration, thus the equivalent velocity $v$can be obtained as $v = v_0 + at_m$, where v_0 is the initial equivalent velocity, t_m is the time, and a is the equivalent

acceleration. Since the change of the equivalent velocity along the azimuth direction is relatively slow, the equivalent acceleration a is generally a small constant value. By integrating the equivalent velocity v from t_c to $t_k + t_{\rm sub}$, the subaperture range model considering the azimuth space-variance of the equivalent velocity caused by the curved orbit can be expressed as

$$R\left(t_{\rm sub}\right) = \sqrt{{R_B}^2 + \left(\left(v_0\left(t_k + t_{\rm sub}\right) + \frac{1}{2}a\left(t_k + t_{\rm sub}\right)^2\right) - \left[v_0 t_c + \frac{1}{2}a{t_c}^2\right]\right)^2}. \tag{2}$$

The subaperture range model of (2) considering the azimuth space-variance of the equivalent velocity is more accurate than the HRM of (1), but it still has the high-order terms residual compared with the actual range history of the spaceborne SAR due to the curved orbit. According to [32], the fourth-order range model can be used to approximately describe the actual range history of the spaceborne SAR, then the high-order terms residual $\Delta R(t_{\rm sub})$ can be derived by the fourth-order range model as

$$\begin{cases} \Delta R\left(t_{\rm sub}\right) = \beta_3((t_k + t_{sub}) - t_c)^3 + \beta_4((t_k + t_{\rm sub}) - t_c)^4 \\ \beta_3 = \left(c_3 - \frac{a v_0}{2R_B}\right) \\ \beta_4 = \left(c_4 - \frac{a^2}{8R_B} + \frac{{v_0}^4}{8{R_B}^3}\right) \end{cases} \tag{3}$$

where β_3 is the third-order residual coefficient, β_4 is the fourth-order residual coefficient, and c_3 and $c_4$are the high-order terms coefficient of the fourth-order range model. β_3 and $\beta_4$can be computed by (3) with the equivalent velocity, the equivalent acceleration, and the reference range of the scene center. Finally, the new subaperture range model in (2) can be modified by the high-order residual term in (3) as

$$R\left(t_{\rm sub}\right) = \sqrt{{R_B}^2 + \left(\left(v_0\left(t_k + t_{\rm sub}\right) + \frac{1}{2}a\left(t_k + t_{\rm sub}\right)^2\right) - \left[v_0 t_c + \frac{1}{2}a{t_c}^2\right]\right)^2} + \beta_3((t_k + t_{\rm sub}) - t_c)^3 + \beta_4((t_k + t_{\rm sub}) - t_c)^4. \tag{4}$$

By comparing (4) with (1), it can be seen that the azimuth space-variance of the equivalent velocity and the high-order terms of the actual range history that are caused by the curved orbit are taken into account in (4). And thus, the *k*th subaperture signal model based on the new subaperture range model is

$$\begin{aligned} s_k\left(t, t_{\rm sub}\right) &= w_r\left(t - \frac{2R\left(t_{\rm sub}\right)}{c}\right) w_{\rm a}\left(t_k + t_{\rm sub}\right) exp\left(-j\frac{4\pi}{\lambda}R\left(t_{\rm sub}\right)\right) \\ &\quad \times \exp\left(j\pi\gamma\left(t - \frac{2R\left(t_{\rm sub}\right)}{c}\right)^2\right) \end{aligned} \tag{5}$$

where $w_r(\cdot)$ is the window function of the linear frequency modulation (LFM) signal, $w_{\rm a}(\cdot)$ is the beam window function, and they are assumed to be the rectangular windows in the formula derivation, t is the range time, λ is the wavelength, γ is the chirp rate of the transmitted signal, and c is the propagation velocity of the light.

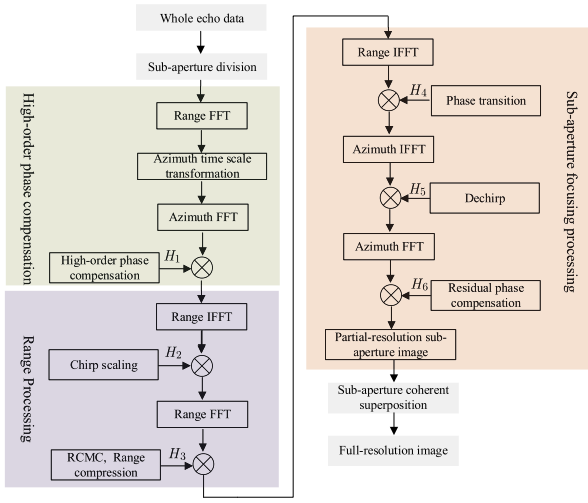

Fig. 3. Algorithm flow chart.

III. High-Resolution Real-Time Imaging Processing

The algorithm flowchart is shown in Fig. 3, which mainly includes the higher order phase compensation, the range processing, the subaperture focusing processing, and the subaperture coherent superposition in image domain. The data are first divided into subapertures to avoid the azimuth spectrum aliasing of the spaceborne spotlight SAR signal. Then, according to the new subaperture range model considering the curved orbit, the azimuth space-variance of the equivalent velocity can be eliminated by azimuth time scale transformation and higher order phase compensation. After using CSA to complete the range processing, the phase transition function is introduced to convert the hyperbolic azimuth phase to the quadratic phase and eliminate the range space-variance of the equivalent velocity. And then, the dechirp function is used for the subaperture signals to obtain the partial-resolution subaperture images. Finally, these partial-resolution subaperture images can be coherently superposed in image domain to obtain the full-resolution image of the whole echo data.

A. Higher Order Phase Compensation

The subaperture division can avoid the azimuth spectrum aliasing in the spaceborne spotlight SAR. Like the traditional subaperture algorithm in [36], the size of the subaperture used in the proposed algorithm is also $T_{\rm sub} = ({\rm PRF} - B_a)/|K_{\rm rot}|$, where B_a is azimuth bandwidth and $K_{\rm rot}$ is the slope of the varying Doppler centroid introduced by the rotation of the antenna.

After the subaperture division, the subaperture signal in (5) is transformed into the $f_r - t_{\rm sub}$ domain by the range FFT as

$$\begin{aligned} s_k\left(f_r, t_{\rm sub}\right) &= w_r\left(f_r\right) w_{\rm a}\left(t_k + t_{\rm sub}\right) exp\left(-j\pi\frac{{f_r}^2}{\gamma}\right) \\ &\quad \times \exp\left(-j\frac{4\pi}{c}\left(f_c + f_r\right) R\left(t_{\rm sub}\right)\right) \end{aligned} \tag{6}$$

where f_r is the range frequency, f_c is the carried frequency, and $R(t_{\rm sub})$ is shown in (4). As the discussion for (4) in the Section II, one can note that the equivalent velocity of the spaceborne SAR varies with the azimuth time, and thus the azimuth space-variance occurs. For eliminating the azimuth space-variance of the equivalent velocity, the method of azimuth time scale transformation is used in the next.

From (4), let

$$v_0\left(t_k+{t_{\rm sub}}'\right)=v_0\left(t_k+t_{\rm sub}\right)+\frac{1}{2}a(t_k+t_{\rm sub})^2 \tag{7}$$

and further get

$${t_k+t_{\rm sub}}'=(t_k+t_{\rm sub})+\varepsilon(t_k+t_{\rm sub})^2 \tag{8}$$

where $\varepsilon=a/(2v_0)$ is the scale transformation factor. Since the equivalent acceleration a is generally a small constant value and the equivalent velocity of spaceborne SAR is usually several kilometers per second, we can get the scale transformation factor $\varepsilon\ll 1$. And thus according to (4) and (8), the subaperture range model in the new azimuth time ${t_{\rm sub}}'$ domain can be written as

$$\begin{aligned}R\left({t_{\rm sub}}'\right)&=\sqrt{{R_B}^2+\left(v_0\left(t_k+{t_{\rm sub}}'-{t_c}'\right)\right)^2}\\&\quad+\beta_3\left(\frac{2\left(t_k+{t_{\rm sub}}'-{t_c}'\right)}{\sqrt{1+4\varepsilon\left(t_k+{t_{\rm sub}}'\right)}+\sqrt{1+4\varepsilon{t_c}'}}\right)^3\\&\quad+\beta_4\left(\frac{2\left(t_k+{t_{\rm sub}}'-{t_c}'\right)}{\sqrt{1+4\varepsilon\left(t_k+{t_{\rm sub}}'\right)}+\sqrt{1+4\varepsilon{t_c}'}}\right)^4\\&\approx\sqrt{{R_B}^2+\left(v_0\left(t_k+{t_{\rm sub}}'-{t_c}'\right)\right)^2}\\&\quad+\beta_3\left(t_k+{t_{\rm sub}}'-{t_c}'\right)^3+\beta_4\left(t_k+{t_{\rm sub}}'-{t_c}'\right)^4\end{aligned} \tag{9}$$

where ${t_c}'=t_c+\varepsilon{t_c}^2$. One can note that the radical sign term in $R({t_{\rm sub}}')$ is the traditional HRM expression, which illustrates that the equivalent velocity is azimuth invariant after the azimuth time scale transformation.

As long as $R(t_{\rm sub})$ in (6) is transformed into $R({t_{\rm sub}}')$ by the azimuth time scale transformation, the azimuth space-variance of the equivalent velocity can be eliminated in the subaperture signal. Since the doppler center $f_{\rm dc}$ of the subaperture signal in the spaceborne spotlight SAR is not zero, it is necessary to make doppler center compensation for (6) first and then carry out the azimuth time scale transformation for (6) according to (7)–(9), so that the subaperture signal of (6) is transformed into

$$\begin{aligned}s_k\left(f_r,{t_{\rm sub}}'\right)&=w_r\left(f_r\right)w_{\rm a}\left(t_k+{t_{\rm sub}}'\right)exp\left(-j\pi\frac{{f_r}^2}{\gamma}\right)\\&\quad\times\exp\left(-j\frac{4\pi}{c}\left(f_c+f_r\right)R\left({t_{\rm sub}}'\right)\right)\\&\quad\times\exp\left(-j2\pi f_{dc}\left(t_k+{t_{\rm sub}}'\right)\right)\end{aligned} \tag{10}$$

where $f_{\rm dc}=K_{\rm rot}t_k$. For convenience, the ${t_{\rm sub}}'$ and ${t_c}'$ are represented by $t_{\rm sub}$ and t_c, respectively, in the following statement. After performing azimuth FFT for (10), the subaperture signal can be obtained as

$$\begin{aligned}s_k\left(f_r,f_{\rm sub}\right)&=w_r\left(f_r\right)w_{\rm a}\left(f_{\rm sub}+f_{\rm dc}\right)exp\left(-j\pi\frac{{f_r}^2}{\gamma}\right)\\&\quad\exp\left(-j2\pi\left(f_{\rm sub}+f_{\rm dc}\right)\left(t_c-t_k\right)\right)\\&\quad\times\exp\left(-j4\pi R_B\sqrt{\left(\frac{f_c+f_r}{c}\right)^2-\left(\frac{f_{\rm sub}+f_{\rm dc}}{2v_0}\right)^2}\right)\\&\quad\exp\left(-j2\pi f_{\rm dc}t_k\right)\\&\quad\times\exp\left(j\pi\beta_3\frac{{R_B}^3\left(f_c+f_r\right)\left(f_{\rm sub}+f_{\rm dc}\right)^3}{2c{v_0}^6}\right.\\&\quad\left.\left(\sqrt{\left(\frac{f_c+f_r}{c}\right)^2-\left(\frac{f_{\rm sub}+f_{\rm dc}}{2v_0}\right)^2}\right)^{-3}\right)\\&\quad\times\exp\left(-j\pi\beta_4\frac{{R_B}^4(f_c+f_r)(f_{\rm sub}+f_{\rm dc})^4}{4c{v_0}^8}\right.\\&\quad\left.\left(\sqrt{\left(\frac{f_c+f_r}{c}\right)^2-\left(\frac{f_{\rm sub}+f_{\rm dc}}{2v_0}\right)^2}\right)^{-4}\right)\end{aligned} \tag{11}$$

where $f_{\rm sub}$ is the azimuth frequency of the subaperture. Then, the high-order terms residual caused by the curved orbit can be compensated by using the high-order phase compensation function shown in (12):

$$\begin{aligned}H_1\left(f_r,f_{\rm sub}\right)=\exp&\left(-j\pi\beta_3\frac{{R_B}^3\left(f_c+f_r\right)\left(f_{\rm sub}+f_{\rm dc}\right)^3}{2c{v_0}^6}\right.\\&\left.\left(\sqrt{\left(\frac{f_c+f_r}{c}\right)^2-\left(\frac{f_{\rm sub}+f_{\rm dc}}{2v_0}\right)^2}\right)^{-3}\right)\\&\times\exp\left(j\pi\beta_4\frac{{R_B}^4(f_c+f_r)(f_{\rm sub}+f_{\rm dc})^4}{4c{v_0}^8}\right.\\&\left.\left(\sqrt{\left(\frac{f_c+f_r}{c}\right)^2-\left(\frac{f_{\rm sub}+f_{\rm dc}}{2v_0}\right)^2}\right)^{-4}\right).\end{aligned} \tag{12}$$

After the higher order phase compensation completed by multiplying (11) and (12), the subaperture signal is obtained as (13)

$$\begin{aligned}s_k\left(f_r,f_{\rm sub}\right)&=w_r\left(f_r\right)w_{\rm a}\left(f_{\rm sub}+f_{\rm dc}\right)exp\left(-j\pi\frac{{f_r}^2}{\gamma}\right)\\&\quad\times\exp\left(-j4\pi R_B\sqrt{\left(\frac{f_c+f_r}{c}\right)^2-\left(\frac{f_{\rm sub}+f_{\rm dc}}{2v_0}\right)^2}\right)\\&\quad\times\exp\left(-j2\pi\left(f_{\rm sub}+f_{\rm dc}\right)\left(t_c-t_k\right)\right)exp\left(-j2\pi f_{\rm dc}t_k\right).\end{aligned} \tag{13}$$

B. Range Processing and Subaperture Focusing Processing

This part, the range processing and subaperture focusing processing are required for subaperture signal. First, the Taylor series expansion is performed on f_r of (13), and then the subaperture signal of (14) is obtained by omitting the cubic term and above terms

$$\begin{aligned} & s_k\left(f_r, f_{\mathrm{sub}}\right) \\ & = w_r\left(f_r\right) w_{\mathrm{a}}\left(f_{\mathrm{sub}}+f_{\mathrm{dc}}\right) \exp\left(-j2\pi\left(f_{\mathrm{sub}}+f_{\mathrm{dc}}\right)\left(t_c-t_k\right)\right) \\ & \times \exp\left(-j\frac{2\pi R_B}{v_0}\sqrt{{f_{aM}}^2-\left(f_{\mathrm{sub}}+f_{\mathrm{dc}}\right)^2}\right) exp\left(-j2\pi f_{\mathrm{dc}} t_k\right) \\ & \times \exp\left(-j\pi\frac{{f_r}^2}{\gamma_e}\right) \exp\left(-j\frac{4\pi}{c} R\left(f_{\mathrm{sub}}+f_{\mathrm{dc}}\right) f_r\right) \end{aligned} \tag{14}$$

where $\frac{1}{\gamma_{\mathrm{e}}}=\frac{1}{\gamma}-R_B\frac{2\lambda\left(\left(f_{\mathrm{sub}}+f_{\mathrm{dc}}\right)/f_{aM}\right)^2}{c^2\left(\sqrt{1-\left(\left(f_{\mathrm{sub}}+f_{\mathrm{dc}}\right)/f_{aM}\right)^2}\right)^3}$, $f_{aM}=2v_0/\lambda$, $R(f_{\mathrm{sub}}+f_{\mathrm{dc}})=R_B+\frac{1}{2}R_B(\frac{f_{\mathrm{sub}}+f_{\mathrm{dc}}}{f_{aM}})^2$.

After performing range inverse fast Fourier transform (IFFT) for (14), the subaperture signal can be obtained as

$$\begin{aligned} & s_k\left(t, f_{\mathrm{sub}}\right) \\ & = w_r\left(t\right) w_{\mathrm{a}}\left(f_{\mathrm{sub}}+f_{\mathrm{dc}}\right) \exp\left(-j2\pi\left(f_{\mathrm{sub}}+f_{\mathrm{dc}}\right)\left(t_c-t_k\right)\right) \\ & \times \exp\left(-j\frac{2\pi R_B}{v_0}\sqrt{{f_{aM}}^2-\left(f_{\mathrm{sub}}+f_{\mathrm{dc}}\right)^2}\right) exp\left(-j2\pi f_{\mathrm{dc}} t_k\right) \\ & \times \exp\left(j\pi\gamma_{\mathrm{e}}\left(t-\frac{2R\left(f_{\mathrm{sub}}+f_{\mathrm{dc}}\right)}{c}\right)^2\right). \end{aligned} \tag{15}$$

Then, the range cell migration correction and range compression are carried out using the standard phase functions of the CSA [37] for subaperture signal of (15). And thus, the range processing is finished.

After the range processing, the subaperture focusing processing is performed. Because of the subaperture signal imaging in the frequency domain, it is necessary to remove the hyperbolic azimuth phase in the subaperture signal and replace it with a quadratic phase by using the phase transition function of H_4

$$\begin{aligned} & H_4\left(t, f_{\mathrm{sub}}\right) \\ & = \exp\left(-j\frac{\pi}{K_a}\left(f_{\mathrm{sub}}+f_{\mathrm{dc}}\right)^2\right) exp\left(-j\frac{2\pi}{v_{0,r}} R_B f_{aM}\right) \\ & \times \exp\left(j\frac{2\pi}{v_{0,r}} R_B\sqrt{{f_{aM}}^2-\left(f_{\mathrm{sub}}+f_{\mathrm{dc}}\right)^2}\right) exp\left(j\Theta_\Delta\right) \end{aligned} \tag{16}$$

where Θ_Δ is the residual phase of the CSA [37], $v_{0,r}$ is the equivalent velocity varying with the range cell, $K_a=-2{v_0}^2/\lambda R_{\mathrm{ref}}$ is the azimuth chirp rate, and R_{ref} is the reference range of the scene center. It is worth noting that, because the curved orbit also brings the range space-variance of the equivalent velocity, the initial equivalent velocity varying with the range cell is used in the H_4. Thus, when H_4 is used to remove the hyperbolic azimuth phase, it also eliminates the range space-variance of the equivalent velocity.

Then, the subaperture signal is expressed as (17) after the phase transition

$$\begin{aligned} s_k\left(t, f_{\mathrm{sub}}\right) = & \operatorname{sinc}_r\left(t\right) w_{\mathrm{a}}\left(f_{\mathrm{sub}}+f_{\mathrm{dc}}\right) exp\left(-j2\pi f_{\mathrm{dc}} t_k\right) \\ & \times \exp\left(-j\frac{\pi}{K_a}\left(f_{\mathrm{sub}}+f_{\mathrm{dc}}\right)^2\right) \\ & \times \exp\left(-j2\pi\left(f_{\mathrm{sub}}+f_{\mathrm{dc}}\right)\left(t_c-t_k\right)\right). \end{aligned} \tag{17}$$

After performing azimuth IFFT for (17), the subaperture signal can be obtained as

$$\begin{aligned} s_k\left(t, t_{\mathrm{sub}}\right) = & \operatorname{sinc}_r\left(t\right) w_{\mathrm{a}}\left(t_k+t_{\mathrm{sub}}-t_c\right) \\ & \times \exp\left(j\pi K_a\left(t_k+t_{\mathrm{sub}}-t_c\right)^2\right) \\ & \times \exp\left(-j2\pi f_{\mathrm{dc}}\left(t_k+t_{\mathrm{sub}}\right)\right). \end{aligned} \tag{18}$$

Acording to (18), the dechirp function of H_5 can be constructed as

$$\begin{aligned} H_5\left(t, t_{\mathrm{sub}}\right) = & \exp\left(-j\pi K_a\left(t_k+t_{\mathrm{sub}}\right)^2\right) \\ & \times \exp\left(j2\pi f_{\mathrm{dc}}\left(t_k+t_{\mathrm{sub}}\right)\right). \end{aligned} \tag{19}$$

After multiplying H_5 by (18), the subaperture signal can be obtained by the azimuth FFT as

$$\begin{aligned} s_k\left(t, f_{\mathrm{sub}}\right) = & \operatorname{sinc}_r\left(t\right) \operatorname{sinc}_{\mathrm{a}}\left(f_{\mathrm{sub}}+K_a t_c\right) \\ & \times \exp\left(j\pi K_a {t_c}^2\right) exp\left(-j2\pi K_a t_c t_k\right). \end{aligned} \tag{20}$$

From the $\operatorname{sinc}_{\mathrm{a}}(f_{\mathrm{sub}}+K_a t_c)$ of (20), we know that the azimuth focusing position of the target is $f_{\mathrm{sub}}=-K_a t_c$. According to the $f_{\mathrm{sub}}=-K_a t_c$, we can compensate for the second phase term of (20). Then, H_6 can be used to complete the azimuth residual phase compensation for (20)

$$H_6\left(t, f_{\mathrm{sub}}\right) = \exp\left(-j2\pi f_{\mathrm{sub}} t_k\right). \tag{21}$$

And thus, the partial-resolution SAR image of the *k*th subaperture data can be obtained as

$$s_k\left(t, f_{\mathrm{sub}}\right) = \operatorname{sinc}_r\left(t\right) \operatorname{sinc}_{\mathrm{a}}\left(f_{\mathrm{sub}}+K_a t_c\right) exp\left(j\pi K_a {t_c}^2\right). \tag{22}$$

C. Subaperture Coherent Superposition in Image Domain

After the partial-resolution subaperture images are obtained, they are then coherently superposed in image domain. From (22), one can note that the subaperture data are focused in the range time domain and azimuth frequency domain, so the image domain is the range time domain and azimuth frequency domain. The subaperture coherent superposition is the key to get a full-resolution image, and the process of the subaperture coherent superposition could be illustrated by the time–frequency diagrams.

As shown in Fig. 4(a), it is assumed that the whole echo data are divided into three subapertures. Each subaperture signal is processed by the proposed algorithm, and the corresponding dechirp function of H_5 is used to complete the subaperture focusing in Fig. 4(b). Fig. 4(c) is the result of each subaperture signal multiplied by the corresponding dechirp function. After performing azimuth FFT on the subaperture signals shown in

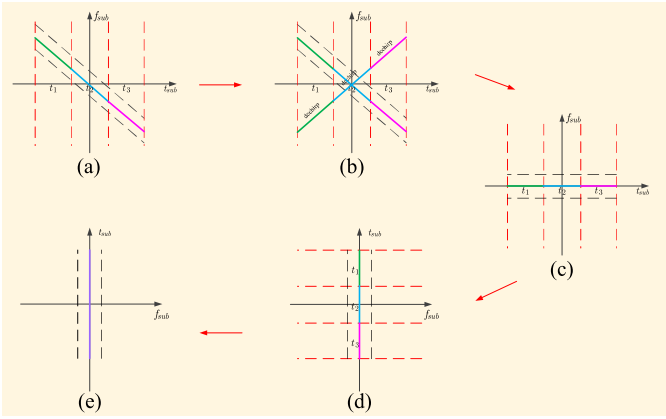

Fig. 4. Process of the subaperture coherent superposition. (a) Subaperture division. (b) Each subaperture signal multiplied by the corresponding dechirp function. (c) Result after the dechirp. (d) Partial-resolution subaperture images. (e) Full-resolution image.

TABLE I
ORBITAL PARAMETERS

Orbital Altitude	531km
Semi-Major Axis	7295.39km
Right Ascension of Ascending Node	219.54°
Inclination	96.74°
Argument of Perigee	78.5°
Mean Anomaly	72.63°
Eccentricity	0.0014

Fig. 4(c) and completing the azimuth residual phase compensation by H_6, each subaperture signal is focused in the azimuth frequency domain, and the partial-resolution subaperture images are obtained in Fig. 4(d). It can be seen from Fig. 4(d) that the focusing position of each subaperture signal on the azimuth frequency axis is the same. Therefore, after the subaperture signals are focused, they can be directly superposed in the image domain without frequency shifting, and the full-resolution image as shown in Fig. 4(e) can be obtained.

IV. EXPERIMENT RESULTS

A. Point Targets Simulation

To verify the effectiveness of the subaperture coherent superposition in the proposed algorithm, the corresponding analysis and point targets simulation of the spaceborne spotlight SAR are presented. In the point targets simulation, the point targets matrix is distributed as the 3×3 (range $\times$ azimuth), the range space and the azimuth space are all 2 km. The subaperture data size is 8192×512 (range $\times$ azimuth) and the subaperture number is 31. In addition, the orbital parameters are listed in Table I and the main system parameters are listed in Table II. According to the orbital parameters, the satellite orbit drawn by using the satellite tool kit software is shown in Fig. 5. The location information of the spaceborne SAR can be obtained by the simulation based on the detailed orbital parameters given in Table I. And then by combining the locations of the point targets and radar system parameters given in Table II, the echo signal can be generated.

TABLE II
SYSTEM PARAMETERS

Wavelength	0.03125m
Bandwidth	400MHz
Sample Frequency	480MHz
Azimuth Bandwidth	23903.12 Hz
PRF	3500Hz
Reference Range	617km
Rotation-Center Range	617km

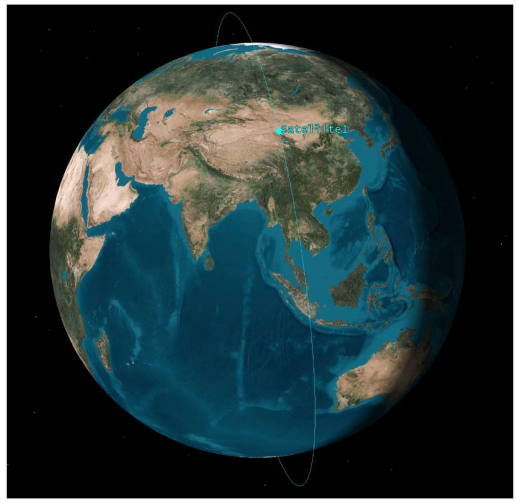

Fig. 5. Satellite orbit drawn by using the STK software.

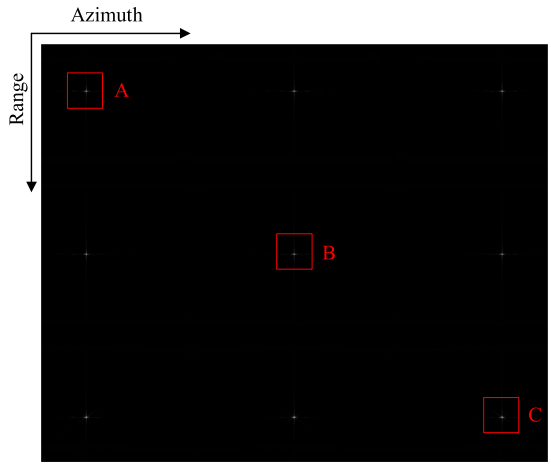

Fig. 6. Point targets simulation results.

Fig. 6 shows the point targets simulation results by using the proposed algorithm. Fig. 7 shows the profiles of the interpolated range spread function and the azimuth spread function of targets A–C denoted in Fig. 6. The focusing qualities of the targets are also evaluated in Table III by computing their peak sidelobe ratio, integrated sidelobe ratio, and impulse response width along range and azimuth, respectively. From Fig. 7 and Table III, one can note that targets A–C are all focused well.

The proposed algorithm can obtain full-resolution image in real time through the coherent superposition of the partial-resolution subaperture images, and thus the subaperture coherent superposition process of the point target B is shown in

TABLE III
MEASURED VALUES OF PSLR, ISLR, AND IRW

	Range			Azimuth		
Points index	PSLR(dB)	ISLR(dB)	IRW (samples)	PSLR(dB)	ISLR(dB)	IRW (samples)
A	-13.2645	-9.8647	1.0035	-13.2667	-9.8673	1.0067
B	-13.2637	-9.8629	1.0032	-13.2624	-9.8617	1.0065
C	-13.2643	-9.8638	1.0034	-13.2659	-9.8668	1.0067

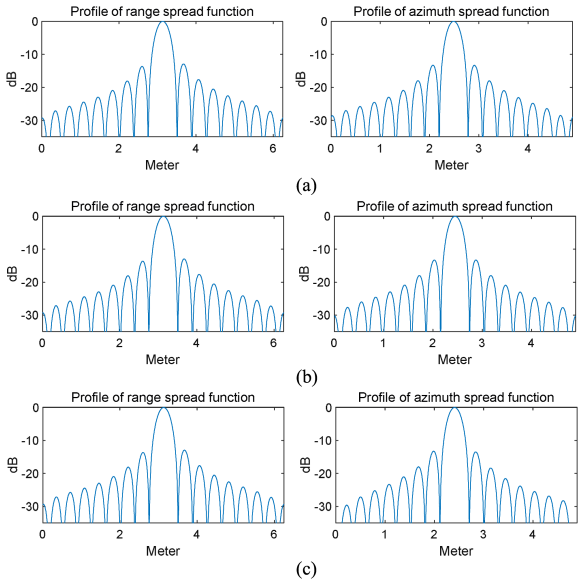

Fig. 7. Profiles of the interpolated range spread function and the azimuth spread function for targets A–C denoted in Fig. 6. (a) Profiles of target A. (b) Profiles of target B. (c) Profiles of target C.

Fig. 8. From Fig. 8(a)–(f), the resolution of the point target B is gradually improved as the subaperture synthesis amount increases, which proves that the proposed subaperture coherent superposition in the image domain can effectively obtain the full-resolution and high-quality image.

B. Surface Targets Simulation

Due to lack of high-resolution spaceborne spotlight SAR data, the surface targets simulation is adopted in this part to further verify the performance of the proposed algorithm. The key to generate the echo of surface targets simulation is how to get the backscattering coefficients of the real SAR image. As we know, in the high-frequency approximation, the backscattering coefficient of each point target can be assumed to be constant with frequency, and the scattering of each point target is all-directional, i.e., the point target scatters the same amount of power in all directions. And then, the gray value of the real SAR image can represent the amplitude of backscattering coefficients. Therefore, we can directly use the gray value of the real SAR image as the backscattering coefficients. In addition, the orbital parameters and radar system parameters in the surface targets simulation are same with that in the point targets simulation. And thus, the backscattering coefficients from the real SAR image and the parameters in Tables I and II are used to generate the echo of the surface targets. After obtaining the echo of the surface targets, it can be processed by the proposed algorithm. In the imaging processing, the echo of the surface targets is divided into 31 subapertures, the subaperture data size is 16 384 $\times$ 512 (range $\times$ azimuth), and the imaging result is shown in Fig. 9(a).

In addition, in order to demonstrate the superiority of the proposed algorithm, the proposed algorithm is compared with another spaceborne spotlight SAR real-time imaging method based on the modified RMA [15]. The echo of the surface targets is processed by the real-time imaging method proposed in [15] and the imaging result is shown in Fig. 9(b). Fig. 10(a) and (b) is the enlarged images of the area marked by the box in Fig. 9(a) and (b). From Figs. 9 and 10, one can note that the focusing quality of the image processed by the proposed algorithm is better than that processed by the real-time imaging method proposed in [15]. This indicates that, compared with the real-time imaging method proposed in [15] without considering the curved orbit, the proposed algorithm in this article considering the curved orbit is more suitable for high-resolution real-time imaging of spaceborne spotlight SAR.

The core of the proposed algorithm is the subaperture coherent superposition in image domain. Therefore, the subaperture coherent superposition process of Fig. 10(a) is shown in Fig. 11. From Fig. 11(a)–(f), the resolution of the scene is gradually improved as the subaperture synthesis amount increases, which proves that the proposed algorithm can effectively obtain the full-resolution and high-quality image.

C. Real-Time Performance Analysis

1) Computational Complexity Analysis: The algorithm in [32] is the traditional subaperture algorithm shown in Fig. 1(a), so the computational complexity of the algorithm in [32] is compared with that of the proposed algorithm in this section.

In the computational complexity analysis, assume that the SAR data has N_r range samples and N_a azimuth samples. Then, the computational complexity of one azimuth FFT/IFFT is $\frac{N_a}{2}\log_2 N_a$, one range FFT/IFFT is $\frac{N_r}{2}\log_2 N_r$, and one phase multiplication is $N_r N_a$. In addition, the length of the interpolation kernel is L, and thus the computational complexity of an interpolation operation is LN_rN_a [38]. Both the proposed algorithm and the algorithm in [32] use subaperture processing, thus assume that the subaperture number is N, and then the azimuth samples of each subaperture data are N_a/N.

According to [32], we can get the algorithm in [32] including four azimuth FFT/IFFTs, two range FFT/IFFTs, six phase multiplications, and three interpolation operations, where two azimuth FFT/IFFTs, two range FFT/IFFTs, four phase multiplications, and three interpolation operations are performed before the subaperture recombination, two azimuth FFT/IFFTs and

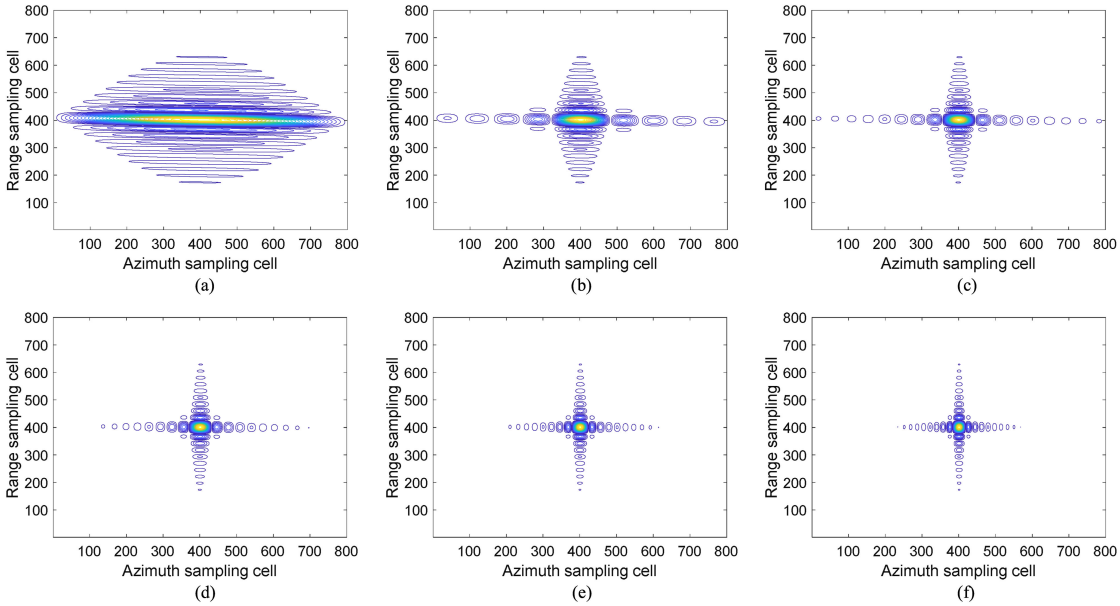

Fig. 8. Subaperture coherent superposition process of the point target B (a) with 1 subaperture data, (b) with 7 subaperture data, (c) with 13 subaperture data, (d) with 19 subaperture data, (e) with 25 subaperture data, and (f) with 31 subaperture data.

TABLE IV
IMAGING PROCESSING TIME OF ONE SUBAPERTURE DATA

Data	Sub-Aperture Data Size (range × azimuth)	Imaging Processing Time of the Last Sub-Aperture Data
Spotlight SAR Data of Point Targets Simulation in Section IV.A	8192 × 512	0.2893s
Spotlight SAR Data of Surface Targets Simulation in Section IV.B	16384 × 512	0.6798s

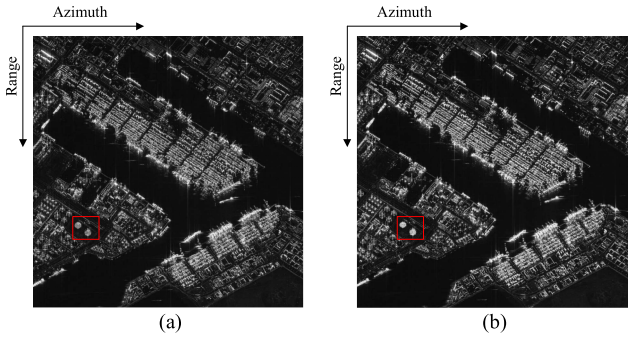

Fig. 9. Imaging results of the surface targets simulation. (a) Imaging result processed by the proposed algorithm in this article. (b) Imaging result processed by the real-time imaging method proposed in [15].

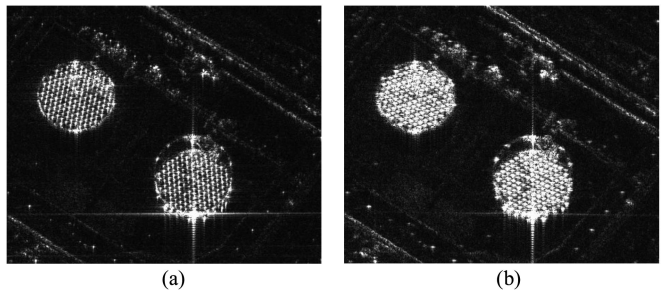

Fig. 10. Enlarged images of the area marked by the box in Fig. 9(a) and (b). (a) Enlarged image of the marked area in Fig. 9(a). (b) Enlarged image of the marked area in Fig. 9(b).

two phase multiplications are performed after the subaperture recombination. And thus, the computational complexity of the algorithm in [32] is calculated as (23).

$$\left(2N_r\frac{N_a}{2N}\log_2\frac{N_a}{N}+2\frac{N_a}{N}\frac{N_r}{2}\log_2 N_r+4\frac{N_a}{N}N_r+3L\frac{N_a}{N}N_r\right)$$
$$N+2N_r\frac{N_a}{2}\log_2 N_a+2N_aN_r$$
$$=N_rN_a\log_2\frac{N_a}{N}+N_aN_r\log_2 N_r+6N_aN_r$$
$$+3LN_aN_r+N_rN_a\log_2 N_a. \quad (23)$$

In the actual SAR data processing by using the proposed algorithm, the azimuth time scale transformation can be completed by the interpolation operation. And thus, from the algorithm flow chart of the proposed algorithm, one can note that three azimuth

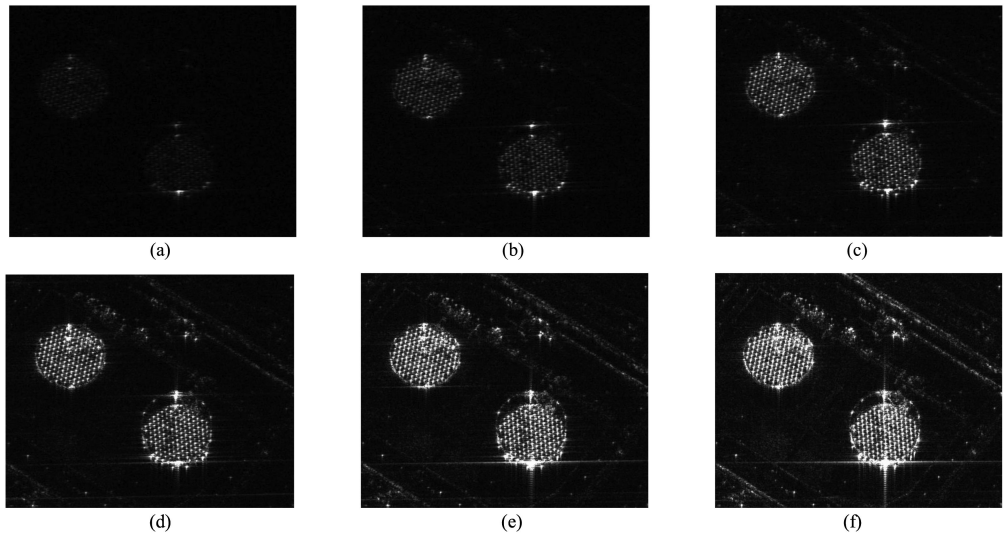

Fig. 11. Subaperture coherent superposition process of Fig. 10(a). (a) with 1 subaperture data, (b) with 7 subaperture data, (c) with 13 subaperture data, (d) with 19 subaperture data, (e) with 25 subaperture data, and (f) with 31 subaperture data.

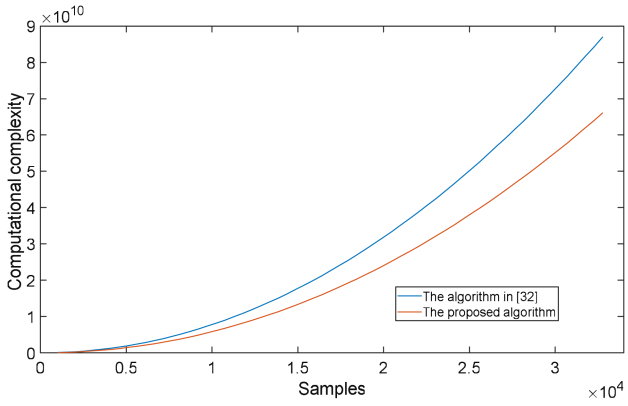

Fig. 12. Computational complexity analysis.

FFT/IFFTs, four range FFT/IFFTs, six phase multiplications, and one interpolation operation are included in each subaperture processing. Thus, the computational complexity of the proposed algorithm is calculated as (24)

$$\left(3N_r\frac{N_a}{2N}\log_2\frac{N_a}{N}+4\frac{N_a}{N}\frac{N_r}{2}\log_2 N_r+6\frac{N_a}{N}N_r+L\frac{N_a}{N}N_r\right)N = \frac{3}{2}N_rN_a\log_2\frac{N_a}{N}+2N_aN_r\log_2 N_r+6N_aN_r+LN_aN_r. \tag{24}$$

For simplicity, we assume that $N_r = N_a$, the azimuth samples of each subaperture signal are 512, and the length of the interpolation kernel $L = 12$. And thus, the computational complexities of the two algorithms are simulated and shown in Fig. 12. From Fig. 12, one can note that the computational complexity of the proposed algorithm is smaller than that of the algorithm in [32], which shows that the proposed algorithm is more effective in real-time processing.

2) DSP Experiment: As we have discussed before, each subaperture data is processed independently by the proposed algorithm to obtain a partial-resolution subaperture image, and then these subaperture images are coherently superimposed in image domain to obtain a final full-resolution image. In order to obtain the final full-resolution image as soon as possible after all the spaceborne spotlight SAR data are recorded, the proposed algorithm adopts the idea that the subaperture data recording and subaperture real-time imaging processing are synchronized. In other words, the real-time imaging processing of the current subaperture data will be completed within the recording time of the next subaperture data. Thus, when all the data have been recorded, only the last subaperture data remains to be processed, and the final full-resolution image can be obtained as long as waiting for the imaging processing time of the last subaperture data.

To record the waiting time needed to obtain the final full-resolution image after all the data have been recorded, the imaging processing time of the last subaperture data that are from the point targets simulation of Section IV-A and the surface targets simulation of Section IV-B are recorded in Table IV by using the TMS320C6678 DSP. It can be seen from Table IV that the final full-resolution image can be obtained only after a few tenths of a second. It is worth mentioning that the processing time given in Table IV is obtained by only using one TMS320C6678 DSP, which proves that the proposed algorithm can be accelerated by using the hardware. In the practical applications, the multicores parallel processing and multiple DSP chips can be used in the on-board real-time imaging processing to further improve the processing speed, making the processing time less than the raw data sampling time. Therefore, the proposed algorithm has good real-time performance.

V. Conclusion

In this article, the new subaperture signal model considering the curved orbit has been established and the formulas derivation of the proposed algorithm has been presented in detail. The

proposed algorithm can solve three main problems including the azimuth spectrum aliasing, the curved orbit, and the real-time performance for the high-resolution real-time imaging processing of the spaceborne spotlight SAR. In the proposed algorithm, the echo data are first divided into subapertures, and the azimuth spectrum aliasing is avoided because the azimuth signal bandwidth of each subaperture data is much smaller than the PRF. Then, the method of azimuth time scale transformation and higher order phase compensation are used to eliminate the azimuth space-variance of the equivalent velocity. After the range processing performed by the CSA, the phase transition function is introduced to convert the hyperbolic azimuth phase to the quadratic phase and eliminate the range space-variance of the equivalent velocity. And then, the dechirp function is used for the subaperture signals to obtain the partial-resolution subaperture images. Finally, these partial-resolution subaperture images are coherently superposed in the image domain to obtain the full-resolution image. Moreover, the proposed algorithm improves the real-time performance by adopting the idea that the subaperture data recording and subaperture real-time imaging processing are synchronized. And after all the data have been recorded, it can shorten the waiting time of obtaining the final full-resolution imaging result to the imaging processing time of the last subaperture data, which greatly accelerates the acquisition of the final full-resolution imaging result and effectively realizes the real-time imaging processing. In the end, the simulations and the real-time performance analysis are performed to validate the proposed algorithm.

REFERENCES

[1] G.-C. Sun, Y. Liu, J. Xiang, W. Liu, M. Xing, and J. Chen, "Spaceborne synthetic aperture radar imaging algorithms: An overview," *IEEE Geosci. Remote Sens. Mag.*, to be published, doi: 10.1109/MGRS.2021.3097894.

[2] J. Chen, G. C. Sun, M. Xing, J. Yang, Z. Li, and G. Jing, "A two-dimensional beam-steering method to simultaneously consider Doppler centroid and ground observation in GEOSAR," *IEEE J. Sel. Topics Appl. Earth Observ. Remote Sens.*, vol. 10, no. 1, pp. 161–167, Jan. 2017.

[3] Y. Xiong, B. Liang, H. Yu, J. Chen, Y. Jin, and M. Xing, "Processing of bistatic SAR data with nonlinear trajectory using a controlled-SVD algorithm," *IEEE J. Sel. Topics Appl. Earth Observ. Remote Sens.*, vol. 14, pp. 5750–5759, May 2021.

[4] Y. Wu, G. C. Sun, X. G. Xia, M. Xing, J. Yang, and Z. Bao, "An azimuth frequency non-linear chirp scaling (FNCS) algorithm for TOPS SAR imaging with high squint angle," *IEEE J. Sel. Topics Appl. Earth Observ. Remote Sens.*, vol. 7, no. 1, pp. 213–221, Jan. 2014.

[5] P. Xiao, W. Guo, Y. Wu, and B. Liu, "A comprehensive method of ambiguity suppression for constellation of geostationary and low earth orbit SAR," *IEEE J. Sel. Topics Appl. Earth Observ. Remote Sens.*, vol. 13, pp. 3327–3335, Jun. 2020.

[6] A. Moreira, P. Prats-Iraola, M. Younis, G. Krieger, I. Hajnsek, and K. P. Papathanassiou, "A tutorial on synthetic aperture radar," *IEEE Geosci. Remote Sens. Mag.*, vol. 1, no. 1, pp. 6–43, Mar. 2013.

[7] A. Moreira, "A golden age for spaceborne SAR systems," in *Proc. 20th Int. Conf. Microw., Radar Wireless Commun.*, 2014, pp. 1–4.

[8] L. W. Mdakane and W. Kleynhans, "An image-segmentation-based framework to detect oil slicks from moving vessels in the Southern African oceans using SAR imagery," *IEEE J. Sel. Topics Appl. Earth Observ. Remote Sens.*, vol. 10, no. 6, pp. 2810–2818, Jun. 2017.

[9] X. M. Li, T. Jia, and D. Velotto, "Spatial and temporal variations of oil spills in the north sea observed by the satellite constellation of TerraSAR-X and TanDEM-X," *IEEE J. Sel. Topics Appl. Earth Observ. Remote Sens.*, vol. 9, no. 11, pp. 4941–4947, Nov. 2016.

[10] S. Suchandt and H. Runge, "Ocean surface observations using the TanDEM-X satellite formation," *IEEE J. Sel. Topics Appl. Earth Observ. Remote Sens.*, vol. 8, no. 11, pp. 5096–5105, Nov. 2015.

[11] M. Martorella, D. Pastina, F. Berizzi, and P. Lombardo, "Spaceborne radar imaging of maritime moving targets with the Cosmo-SkyMed SAR System," *IEEE J. Sel. Topics Appl. Earth Observ. Remote Sens.*, vol. 7, no. 7, pp. 2797–2810, Jul. 2014.

[12] J. Krecke, M. Villano, N. Ustalli, A. C. M. Austin, J. E. Cater, and G. Krieger, "Detecting ships in the New Zealand exclusive economic zone: Requirements for a dedicated SmallSat SAR mission," *IEEE J. Sel. Topics Appl. Earth Observ. Remote Sens.*, vol. 14, pp. 3162–3169, Mar. 2021.

[13] F. Zhang, X. Yao, H. Tang, Q. Yin, Y. Hu, and B. Lei, "Multiple mode SAR raw data simulation and parallel acceleration for Gaofen-3 mission," *IEEE J. Sel. Topics Appl. Earth Observ. Remote Sens.*, vol. 11, no. 6, pp. 2115–2126, Jun. 2018.

[14] R. Que, O. Ponce, S. V. Baumgartner, and R. Scheiber, "Multi-mode real-time SAR on-board processing," in *Proc. 11th Eur. Conf. Synthetic Aperture Radar*, 2016, pp. 1–6.

[15] F. Zhou, J. Yang, G. Sun, and J. Zhang, "A real-time imaging processing method based on modified RMA with sub-aperture images fusion for spaceborne spotlight SAR," in *Proc. IEEE Int. Geosci. Remote Sens. Symp.*, 2020, pp. 1905–1908.

[16] J. Chen, J. Zhang, Y. Jin, H. Yu, B. Liang, and D. G. Yang, "Real-time processing of spaceborne SAR data with nonlinear trajectory based on variable PRF," *IEEE Trans. Geosci. Remote Sens.*, vol. 60, Apr. 2022, Art. no. 5205212.

[17] L. Sun, Z. Yu, C. Li, W. Liu, S. Wang, and J. Geng, "An imaging algorithm for spaceborne high-squint L-band SAR based on time-domain rotation," *IEEE J. Sel. Topics Appl. Earth Observ. Remote Sens.*, vol. 12, no. 12, pp. 5289–5299, Dec. 2019.

[18] D. Liang *et al.*, "Processing of very high resolution GF-3 SAR spotlight data with non-start–stop model and correction of curved orbit," *IEEE J. Sel. Topics Appl. Earth Observ. Remote Sens.*, vol. 13, pp. 2112–2122, May 2020.

[19] X. Jing and Y. Guo, "Design of spotlight SAR Imaging system based on multicore DSP," in *Proc. 6th Asia-Pacific Conf. Synthetic Aperture Radar*, 2019, pp. 1–4.

[20] Y. Cao, G. Sun, M. Du, M. Xing, L. Guo, and J. Yang, "Intersatellite cloud computing system for GF-3 SAR data real-time processing," in *Proc. 6th Asia-Pacific Conf. Synthetic Aperture Radar*, 2019, pp. 1–4.

[21] Z. Ding *et al.*, "A modified fixed-point chirp scaling algorithm based on updating phase factors regionally for spaceborne SAR real-time imaging," *IEEE Trans. Geosci. Remote Sens.*, vol. 56, no. 12, pp. 7436–7451, Dec. 2018.

[22] G. Sun, Y. Liu, M. Xing, S. Wang, L. Guo, and J. Yang, "A real-time imaging algorithm based on sub-aperture CS-dechirp for GF3-SAR data," *Sensors*, vol. 18, no. 8, 2018, Art. no. 2562.

[23] G. Sun, M. Xing, X. Xia, Y. Wu, and Z. Bao, "Beam steering SAR data processing by a generalized PFA," *IEEE Trans. Geosci. Remote Sens.*, vol. 51, no. 8, pp. 4366–4377, Aug. 2013.

[24] W. G. Carrara, R. S. Goodman, and M. A. Ricoy, "New algorithms for widefield SAR image formation," in *Proc. IEEE Radar Conf.*, 2004, pp. 38–43.

[25] N. Xin, S. Shijian, Y. Hui, L. Ying, Z. Long, and L. Wanming, "A wide-field SAR polar format algorithm based on quadtree sub-image segmentation," in *Proc. IEEE Int. Geosci. Remote Sens. Symp.*, 2018, pp. 9355–9358.

[26] R. Lanari, M. Tesauro, E. Sansosti, and G. Fornaro, "Spotlight SAR data focusing based on a two-step processing approach," *IEEE Trans. Geosci. Remote Sens.*, vol. 39, no. 9, pp. 1993–2004, Sep. 2001.

[27] G. Sun, M. Xing, X. Xia, J. Yang, Y. Wu, and Z. Bao, "A unified focusing algorithm for several modes of SAR based on FrFT," *IEEE Trans. Geosci. Remote Sens.*, vol. 51, no. 5, pp. 3139–3155, May 2013.

[28] J. Mittermayer, A. Moreira, and O. Loffeld, "Spotlight SAR data processing using the frequency scaling algorithm," *IEEE Trans. Geosci. Remote Sens.*, vol. 37, no. 5, pp. 2198–2214, Sep. 1999.

[29] F. He, Q. Chen, Z. Dong, and Z. Sun, "Processing of ultrahigh-resolution spaceborne sliding spotlight SAR data on curved orbit," *IEEE Trans. Aerosp. Electron. Syst.*, vol. 49, no. 2, pp. 819–839, Apr. 2013.

[30] P. Prats-Iraola *et al.*, "On the processing of very high resolution spaceborne SAR data," *IEEE Trans. Geosci. Remote Sens.*, vol. 52, no. 10, pp. 6003–6016, Oct. 2014.

[31] Y. Gao, D. Liang, T. Fang, Z.-X. Zhou, H. Zhang, and R. Wang, "A modified extended wavenumber-domain algorithm for ultra-high resolution spaceborne spotlight SAR data processing," in *Proc. IEEE Int. Geosci. Remote Sens. Symp.*, 2020, pp. 1544–1547.

[32] Y. Wu, G. Sun, C. Yang, J. Yang, M. Xing, and Z. Bao, "Processing of very high resolution spaceborne sliding spotlight SAR data using velocity scaling," *IEEE Trans. Geosci. Remote Sens.*, vol. 54, no. 3, pp. 1505–1518, Mar. 2016.
[33] P. Wang, W. Liu, J. Chen, M. Niu, and W. Yang, "A High-order imaging algorithm for high-resolution spaceborne SAR based on a modified equivalent squint range model," *IEEE Trans. Geosci. Remote Sens.*, vol. 53, no. 3, pp. 1225–1235, Mar. 2015.
[34] B. Zhao, X. Qi, H. Song, R. Wang, Z. Zhang, and H. Jiang, "A new approach for spotlight geosynchronous SAR data focusing," in *Proc. IEEE Int. Geosci. Remote Sens. Symp.*, 2013, pp. 899–902.
[35] A. Moreira, "Real-time synthetic aperture radar (SAR) processing with a new subaperture approach," *IEEE Trans. Geosci. Remote Sens.*, vol. 30, no. 4, pp. 714–722, Jul. 1992.
[36] P. Prats R. Scheiber, J. Mittermayer, A. Meta, and A. Moreira, "Processing of sliding spotlight and TOPS SAR data using baseband Azimuth Scaling," *IEEE Trans. Geosci. Remote Sens.*, vol. 48, no. 2, pp. 770–780, Feb. 2010.
[37] R. K. Raney, H. Runge, R. Bamler, I. G. Cumming, and F. H. Wong, "Precision SAR processing using chirp scaling," *IEEE Trans. Geosci. Remote Sens.*, vol. 32, no. 4, pp. 786–799, Jul. 1994.
[38] W. Liu, G. Sun, X. Xia, J. Chen, L. Guo, and M. Xing, "A modified CSA based on joint time-Doppler resampling for MEO SAR stripmap mode," *IEEE Trans. Geosci. Remote Sens.*, vol. 56, no. 6, pp. 3573–3586, Jun. 2018.

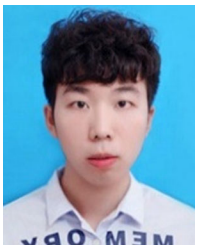

Yanbin Liu (Student Member, IEEE) was born in Inner Mongolia, China, in 1996. He received the B.S. degree in electronic information science and technology from Hefei University of Technology, Hefei, China, in 2017, where he is currently working toward the Ph.D. degree in electronic science and technology at Xidian University, Xi'an, China.

His research interests include synthetic aperture radar imaging.

Guang-Cai Sun (Senior Member, IEEE) received the master's degree in communications engineering from Post and Telecommunication Institution, Xi'an, China, in 2006, and the Ph.D. degree in signal and information processing from Xidian University, Xi'an, China, in 2012.

He is currently a Full Researcher with the National Laboratory of Radar Signal Processing, and also with the Collaborative Innovation Center of Information Sensing and Understanding, Xidian University. He has authored or coauthored one book and published more than 50 papers. His research interests include imaging of several SAR modes, moving target detection, and imaging.

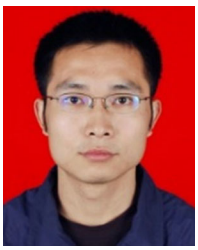

Liang Guo was born in Henan, China, in 1983. He received the B.S. degree in information warfare technology from Xidian University, Xi'an, China, in 2005, and the Ph.D. degree in signal and information processing from Xidian University, Xi'an, China, in 2009.

He is currently a Full Professor with the School of Physics and Optoelectronic Engineering, Xidian University. He has authored or coauthored more than 20 papers. His research interests include imaging of several synthetic aperture radar modes, synthetic aperture radar, and real-time imaging.

Mengdao Xing (Fellow, IEEE) received the B.S. and Ph.D. degrees in signal and information processing from Xidian University, Xi'an, Shaanxi, China, in 1997 and 2002, respectively.

He is currently a Professor with the National Laboratory of Radar Signal Processing, Xidian University. He holds the appointment of Dean with the Academy of Advanced Interdisciplinary Research Department, Xidian University. He has authored or coauthored more than 200 refereed scientific journal papers. He also has authored or coauthored two books about SAR signal processing. The total citation times of his research are greater than 10 000 (H-index 50). He was rated as Most Cited Chinese Researchers by Elsevier. He has achieved more than 50 authorized China patents. His research interests include synthetic aperture radar (SAR), SAR interferometry (InSAR), inversed SAR, sparse signal processing, and microwave remote sensing.

Prof. Xing's research has been supported by various funding programs, such as National Science Fund for Distinguished Young Scholars. He holds several Special Issues on IEEE GRSM and Journal of Selected Topics in Applied Earth Observations and Remote Sensing. He currently serves as the Associate Editors for radar remote sensing of the IEEE TRANSACTIONS ON GEOSCIENCE AND REMOTE SENSING and the Editor-in-Chief of *MDPI Sensors*.

Hanwen Yu (Senior Member, IEEE) received the B.S. and Ph.D. degrees in electronic engineering from Xidian University, Xian, China, in 2007 and 2012, respectively.

He was a Postdoctoral Research Fellow with the Department of Civil and Environmental Engineering, National Center for Airborne Laser Mapping, University of Houston, Houston, TX, USA. He is currently a Full Professor with the School of Resources and Environment, University of Electronic Science and Technology of China, Chengdu, China, and is currently an Adjunct Professor with the Ph.D. School in Information and Communication Technology and Engineering, University of Naples Parthenope, Naples, Italy. He has authored or coauthored more than 40 research articles in high-impact peer-reviewed journals, such as the IEEE TRANSACTIONS ON GEOSCIENCE AND REMOTE SENSING, IEEE TRANSACTIONS ON IMAGE PROCESSING, and *Remote Sensing of Environment*. His research interests include phase unwrapping, machine learning, and synthetic aperture radar interferometry (InSAR) signal processing and applications.

Prof. Yu has reviewed more than 280 manuscripts for more than 20 different journals. He was a recipient of the Recognition of Best Reviewer of the IEEE Transactions on Geoscience and Remote Sensing in 2019. He serves as a Topical Associate Editor in the IEEE TRANSACTIONS ON GEOSCIENCE AND REMOTE SENSING, and an Associate Editor in the IEEE GEOSCIENCE AND REMOTE SENSING MAGAZINE. He has guest edited five special issues on InSAR remote sensing for different journals (e.g., IEEE JOURNAL OF SELECTED TOPICS IN APPLIED EARTH OBSERVATIONS AND REMOTE SENSING and *MDPI Remote Sensing*).

Ruimin Fang was born in Anhui, China, in 1998. He received the bachelor's degree in electronic information engineering from Anhui Normal University, Anhui, China, in 2020. He is currently working toward the master's degree in signal and information processing at Xidian University, Xi'an, China.

His research interests include spaceborne SAR real-time imaging system.

Shiyu Wang received the B.S. degree in physics from Northwest University, Xi'an, China, in 1987, and the Ph.D. degree in electronic science and technology from Xi'an Jiaotong University, Xi'an, China, in 2003.

He is currently a Professor with the School of Physics and Optoelectronic Engineering, Xidian University, Xi'an, China. His research interests include laser and lidar technology.